Final Technical Report

SCIENTIFIC INVESTIGATIONS OF TROPICAL WIND, ENERGY CONVERSION AND REFERENCE LEVEL EXPERIMENT (TWERLE)

NASA Grant NSG 5126

for the period
July 1976 - September 1977

Verner E. Suomi
Principal Investigator

Report prepared by:

William Massman
Barry Hinton
Juris Afanasjevs

University of Wisconsin
Space Science and Engineering Center
Madison, Wisconsin

January 1978

ABSTRACT

This report summarizes the results from the Tropical Winds, Energy Conversion and Reference Level Experiment (TWERLE) for the period July 1976 through 6 September 1977.* These results are:

(1) A latitude profile of the rate of conversion from kinetic to potential energy for the period from 12 June 1975 to 1 August 1976.

(2) Evidence that gravity waves generated in the troposphere systematically deposit energy in the vicinity of the tropopause, and are a mechanism for the dissipation of kinetic energy on the global scale.

(3) Evidence that the jet stream is an important mechanism for generating these waves.

From 10°S to 50°S we found vertical energy fluxes of the order of one watt per square meter, and much smaller values poleward of 50°S. We obtained zonally averaged values of the magnitude of the vertical flux of horizontal momentum on the order of one-half dyne per square centimeter, with a tendency for smaller values south of 30°S. We completed the processing of the data set to insure the scientific integrity of the results. This required careful and extensive examination of individual balloon platforms and their sensors.

Further details on the results described above can be found in Sections 1 and 2 of this report.

1. TWERLE Energy Conversion and Dissipation Studies

A fundamental question of meteorology concerns the conversion of the potential energy inherent in the mass distribution of the atmosphere into the kinetic energy of atmospheric motion. This conversion process is difficult to study directly because of the low thermodynamic efficiency at which it takes place, and because of the wide scale of atmospheric motions over which it can occur (Kung, 1967, 1969).

In general, however, this conversion process can be thought of as work done against the horizontal pressure gradient. This cross isobaric flow then will give the rate at which internal energy is converted into kinetic energy, or vice versa. This term is denoted as $\vec{V} \cdot \nabla_H p$, and is related to the rate of pressure change of an air parcel with respect to time in the following manner:

---

* This work was funded by the National Aeronautics and Space Administration under grant NSG 5126.

$$\frac{dp}{dt} = \frac{\partial p}{\partial t} + \vec{V} \cdot \nabla_H p + w \frac{\partial p}{\partial z} \qquad (1)$$

Direct measurements of this cross isobaric flow term from conventional weather maps of the wind and pressure fields are difficult because of the state of near mechanical balance of atmospheric motion systems; that is, the wind and pressure fields are nearly in geostrophic balance. Previous estimates of energy conversion rates were based on indirect means, dependent on transforming the relevant equations into different forms or estimating frictional dissipation.

In the present work we shall report how this term was measured to a first approximation by a superpressure balloon. Measurements of pressure and altitude on a floating balloon platform can be related to the work term in the following manner:

$$\left(\frac{dp}{dt}\right)_B - w_B \frac{\partial p}{\partial z} = \frac{\partial p}{\partial t} + \vec{V} \cdot \vec{\nabla}_H p \qquad (2)$$

Equation (2) is valid because a superpressure balloon floats on a constant density surface and moves horizontally with the wind at that level. The left hand side of equation (2) can be measured using a constant density balloon, where $(\partial p/\partial t)_B$ represents the rate of pressure change with time as experienced by the balloon and $(w_B \partial p/\partial z)$ is essentially the vertical motion of the balloon.

All that remains to be measured is the local term, $\partial p/\partial t$, which, if integrated over long time periods (say weeks to months), must be smaller than the pressure-work term. Therefore, a direct measure of $\vec{V} \cdot \nabla_H p$ is given simply by the long-term average of the left hand side of equation (2).

The work done by or against the pressure gradient force is the term measured in this experiment; the results are presented in Figure 1. Measurements of the left hand side of equation (2) were accumulated in latitude belts two degrees wide for 420 days of the experiment starting June 13, 1975. We have assumed that the local term is negligible anywhere when averaged over this length of time. The units for the conversion are expressed in watts/(m^2 - 50mb) for the purpose of comparison with previous results. Table 1 gives the numerical values corresponding to Figure 1.

From the equator to about 25°S, very little conversion is noted because the balloons are in the troposphere where little conversion takes place. Between 20° and 30°S the balloons encounter the jet stream and conversion is observed. South of 30°S, the conversion is direct (Potential Energy → Kinetic Energy) to about 33°S, which corresponds to the traditional Hadley cell. From 33°S to about 40°S the conversion is reversed, the indirect circulation corresponding to a Ferrel cell. Finally, the band from about 40°S to 60°S is a region of

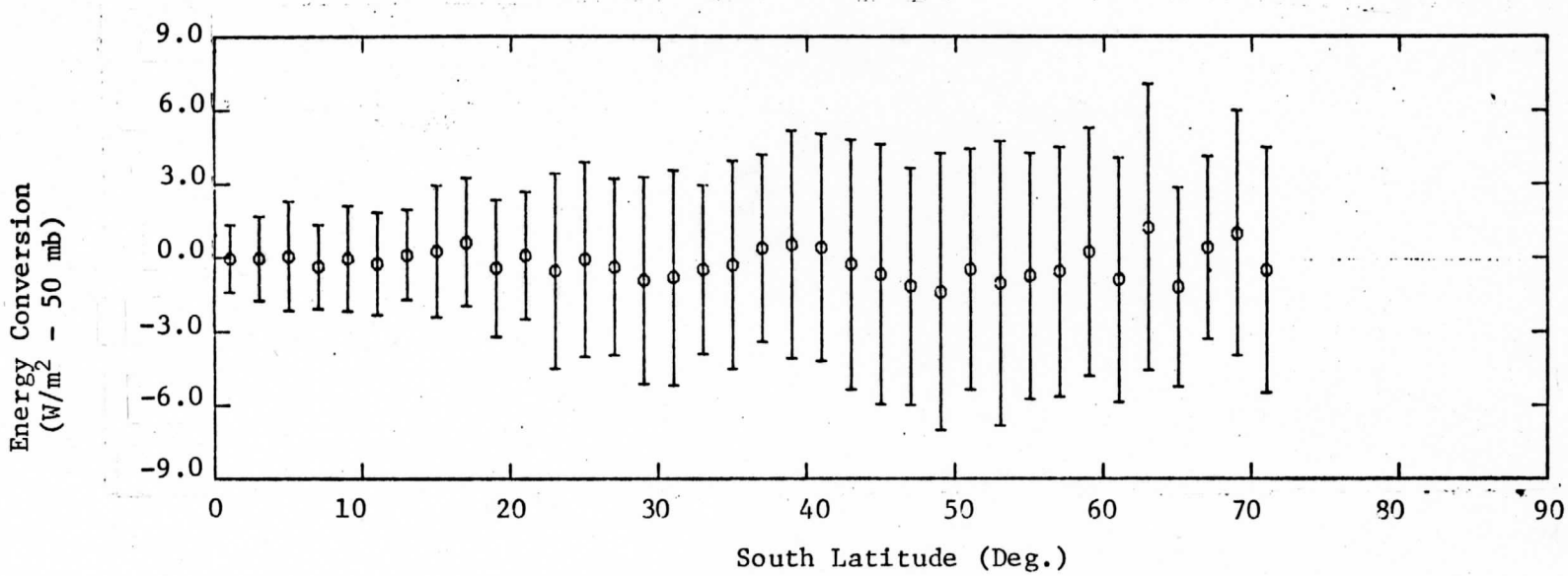

Figure 1. Energy Conversion as a function of latitude for the period 12 June 1975 to 1 August 1976. Positive values represent conversion from kinetic energy to potential energy. Values south of about 65°S are somewhat erratic because of small data samples. Vertical lines through each point represent the rms of all individual measurements of conversion and hence, reflect the natural variability of the atmosphere and not necessarily the error.

Table 1:

Energy Conversion Values for 12 June 1975 to 1 August 1976

Latitude Belt	Conversion (W/m^2 - 50 mb)†	Number of Observations
Eq - 2S	.01	68
2S - 4S	-.07	151
4S - 6S	-.02	160
6S - 8S	.13	176
8S - 10S	-.08	278
10S - 12S	-.08	320
12S - 14S	-.07	303
14S - 16S	-.37	257
16S - 18S	-.07	228
18S - 20S	-.15	241
20S - 22S	-.07	235
22S - 24S	-.61	243
24S - 26S	-.23	267
26S - 28S	-.53	286
28S - 30S	-.82	292
30S - 32S	-.02	253
32S - 34S	.02	263
34S - 36S	-.32	289
36S - 38S	.46	348
38S - 40S	.16	334
40S - 42S	-.31	306
42S - 44S	-.19	334
44S - 46S	-.22	315
46S - 48S	-.97	331
48S - 50S	-.67	288
50S - 52S	-.37	302
52S - 54S	-.50	298
54S - 56S	-.29	275
56S - 58S	-.12	222
58S - 60S	.06	202
60S - 62S	-.27	150
62S - 64S	.38	112
64S - 66S	-.80	68
66S - 68S	-.36	56
68S - 70S	-.44	23
70S - 72S	-.91	21

† Conversion units are Watts/meter^2 in a 50 mb thick layer.

direction conversion again. South of 60°S there are not enough observations to be sure of the exact nature of the conversion.

We used only the highest quality data in obtaining these results. Comparisons with previous values for the conversion (Kung, 1967, 1969) show very good agreement. Kung observed the maximum conversion of .4w/(m^2- 50mb)(at roughly 45°N and 150 mb level above the United States); we observed .7w/(m^2 - 50mb) at about 45°S at the same level.

2. TWERLE Gravity Wave Studies

Previous Studies

Atmospheric gravity waves are quite common and those similar to ocean surface waves have been known for a century; only in the past few years, however, has their importance to atmospheric dynamics become evident. On a subsynoptic scale these waves can be mechanisms for the initiation of thunderstorms or clear-air turbulence. On a larger synoptic or global scale they are important in the transport of energy and momentum (Eliassen and Palm, 1960). Under a variety of atmospheric conditions these waves can exchange energy and momentum directly with the mean flow and therefore can cause velocity changes in the mean flow. They can also be generated by the jet stream and therefore act as a drag force on the mean flow in much the same way as mountain generated lee waves. This drag force--at least that component induced by stationary mountain lee waves (more or less fixed in space and persistent in time)--accounts for half of the difference between the observed and computed wind speeds of the jet stream. The effects of traveling internal waves (more or less random in both space and time) on the general circulation, however, is less well understood.

In 1974, test flights demonstrated that a constant density balloon equipped with an altimeter and pressure sensor could be used to compute vertical fluxes of energy and horizontal momentum associated with gravity waves in a region of the atmosphere where divergence or convergence of these fluxes is important. In the past the divergence or convergence of these wave associated fluxes have been studied either in simple isolated cases (Hooke and Hardy, 1974; Gossard, 1962) or in a few mountainous regions (Bretherton, 1969; Lilly and Kennedy, 1973); free floating constant density balloons, however, make it possible to observe waves generated by many sources on a global scale.

Studies Using TWERLE

The TWERL Gravity Wave Experiment draws upon two data sources. The primary data source is a global data set provided by eight specially adapted TWERL balloons modified to allow for data storage. This data set--to be called "memory unit data" was obtained from free floating

balloons which averaged every eight readings for each of the three sensors then stored the data sequentially about every nine minutes. (See Appendix A for details.) The memory unit balloons provided 526 time series and the locations at which each series was taken. Figure 2 shows the total set of observations obtained with the eight memory balloons; of these, 200 were identified as gravity wave observations and are shown in Figure 3.

The secondary source is taken from data recorded on the ground at the time of launch of all normal TWERL balloons from the time they reached altitude until they drifted out of range of the launch site receiver. Hence this data is more restricted geographically than the memory unit data. This set will be called "first day data," consisting of about 400 time series of simultaneous readings of temperature, pressure and geometric altitude recorded once per minute. This set provided 31 gravity wave observations, limited to small geographical regions, near the launch sites. (see Figure 4).

To find these gravity waves, a linear regression was done on each time series to remove any trend, then each was filtered to check for wave motions. The band-pass filter removes low frequency motions corresponding to the diurnal oscillation of the balloon, as well as high frequency oscillations corresponding to the balloon's neutral buoyant oscillation (NBO) and atmospheric Brunt-Väiäsalla motions. The high frequency cutoff is about .055 cycles/min. The period of the filtered data showing a wave almost always agreed with that period corresponding to a peak in the spectrum computed by a fast Fourier transform on the unfiltered time series.

There are three criteria for deciding if an observation shows a valid gravity wave. First, there must be a periodic motion in the filtered altimeter trace to which a single frequency can be assigned; second, when corrected for filtering, the sensor data showing a wave motion must have an amplitude greater than the resolution of the instruments; and third, the amplitude from one cycle to the next should be approximately (but not necessarily exactly) the same.

Figure 5 is an example of gravity wave data extracted by this method, taken from flight 0376 launched 8 December 1975 from Christchurch, New Zealand. The variance spectra of the sensors for this flight are given in Figure 6. Each has a maximum at .026 cycles/min (period = 38 minutes) and corresponds to a traveling wave having the same intrinsic frequency. Figure 7 clearly shows this wave motion in the filtered sensor traces for the flight.

The smoothed data is used to determine the vertical fluxes of energy and horizontal momentum. The balloon's equation of motion is solved numerically to obtain $w'(t)$; the pressure perturbation $p'(t)$ is found by subtracting from the smoothed pressure trace both the average

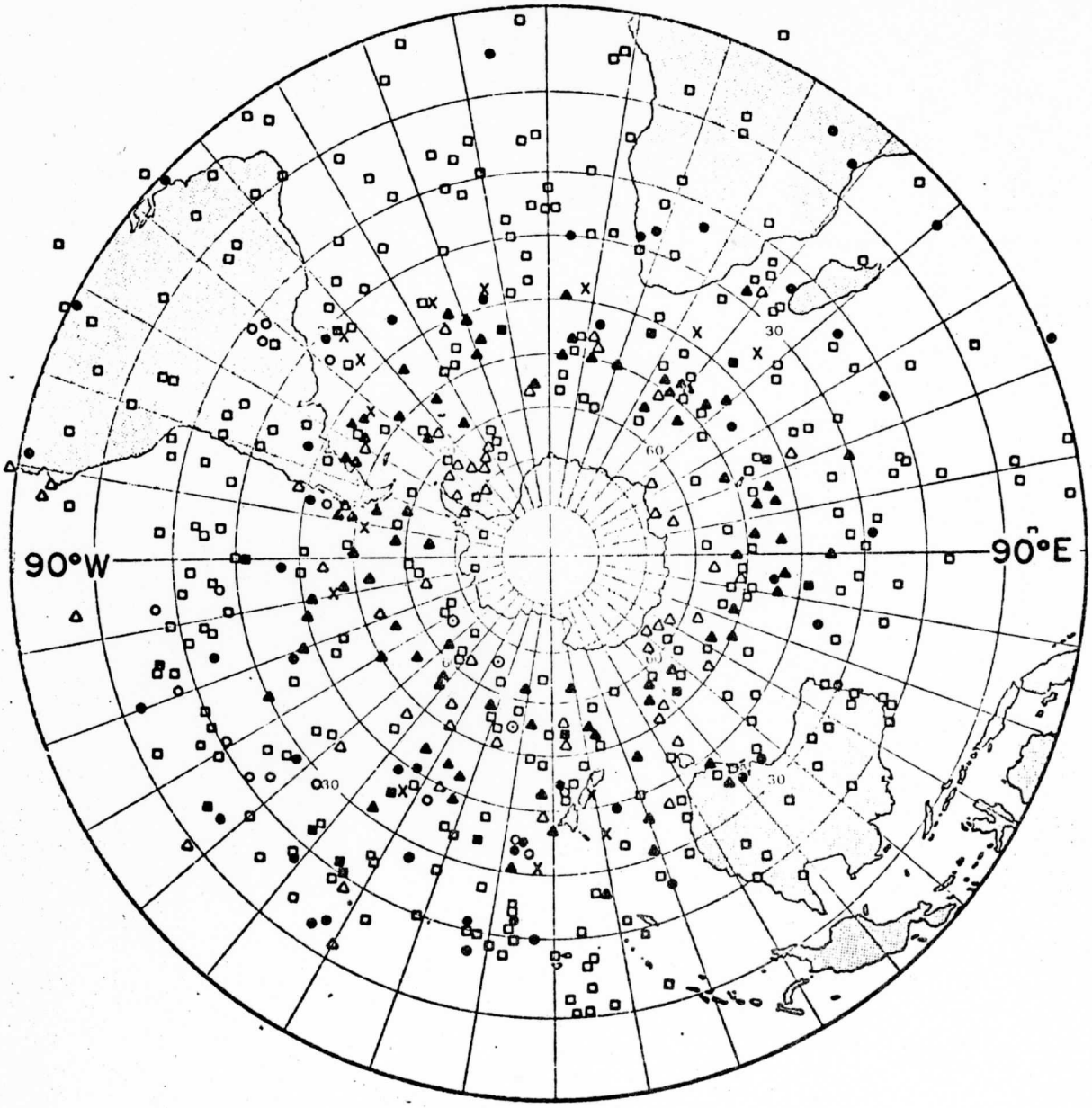

Figure 2. Geographical distribution of observations from the eight memory balloons for the period 3 December 1975 to 16 November 1976. Each point represents a contact with Nimbus 6 during which several hours of data was successfully stored and transmitted.

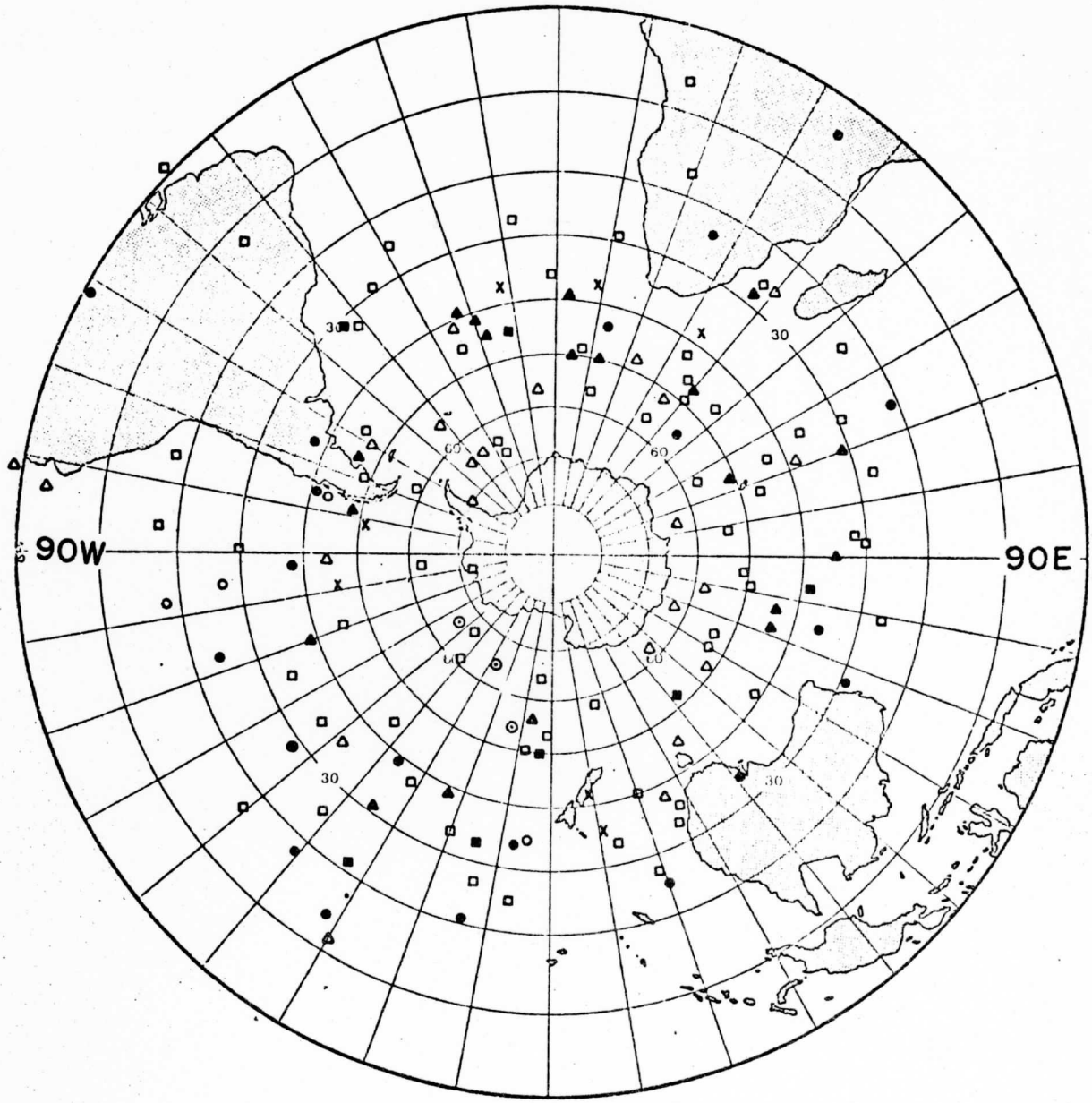

Figure 3. Geographical distribution of gravity wave observations derived from the total set of observations illustrated in Fig. 2.

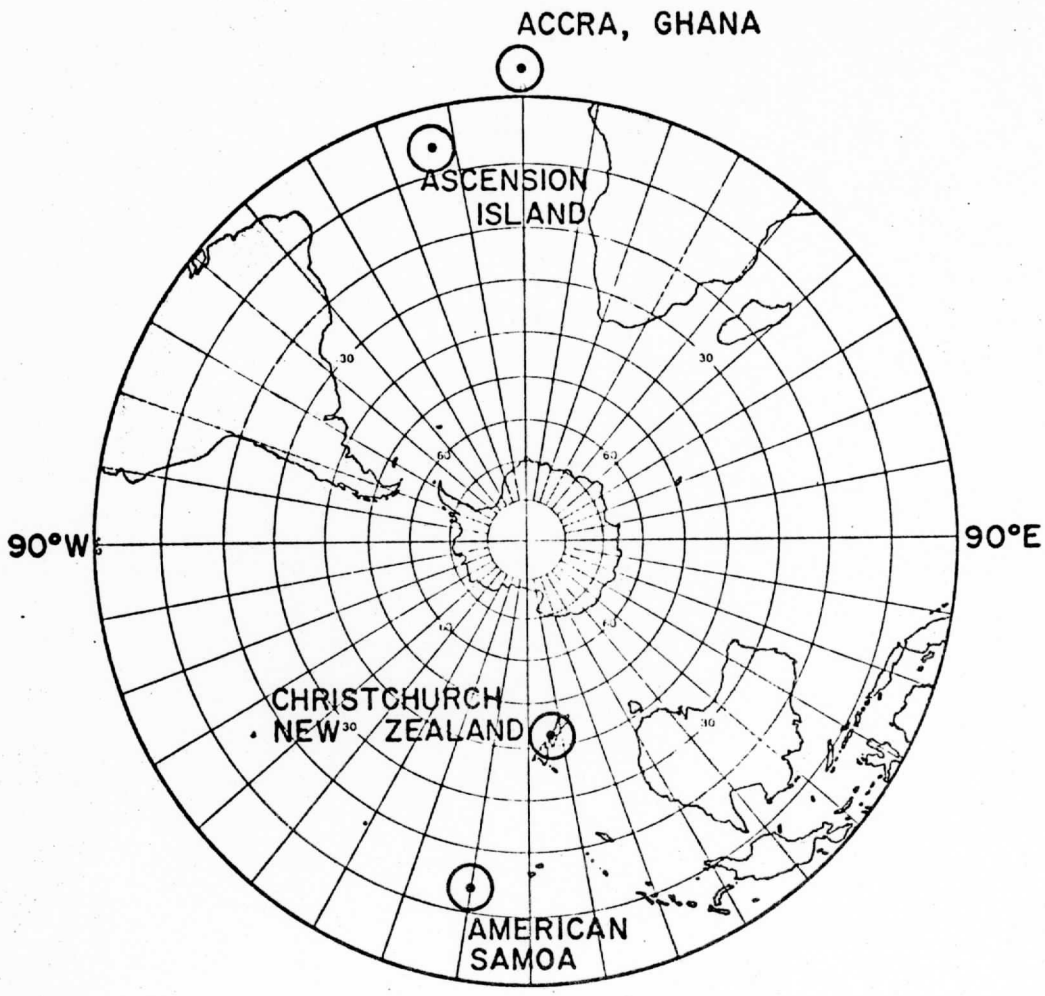

Figure 4. Launch sites where 'first day data sets' were gathered. Circle around each station is about 400 km radius.

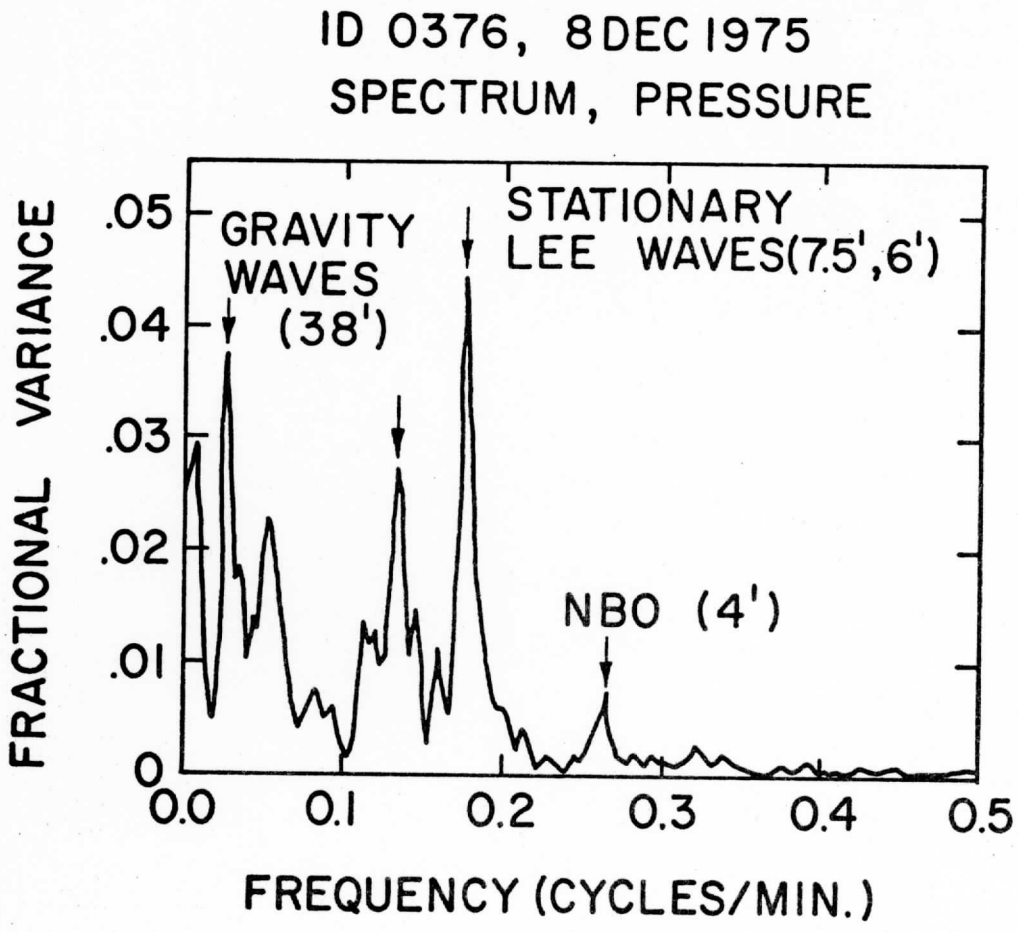

Figure 5. Unfiltered spectrum of normalized variance of pressure for platform 0376 on 8 December 1975. Identification and periods are given for the prominent peaks.

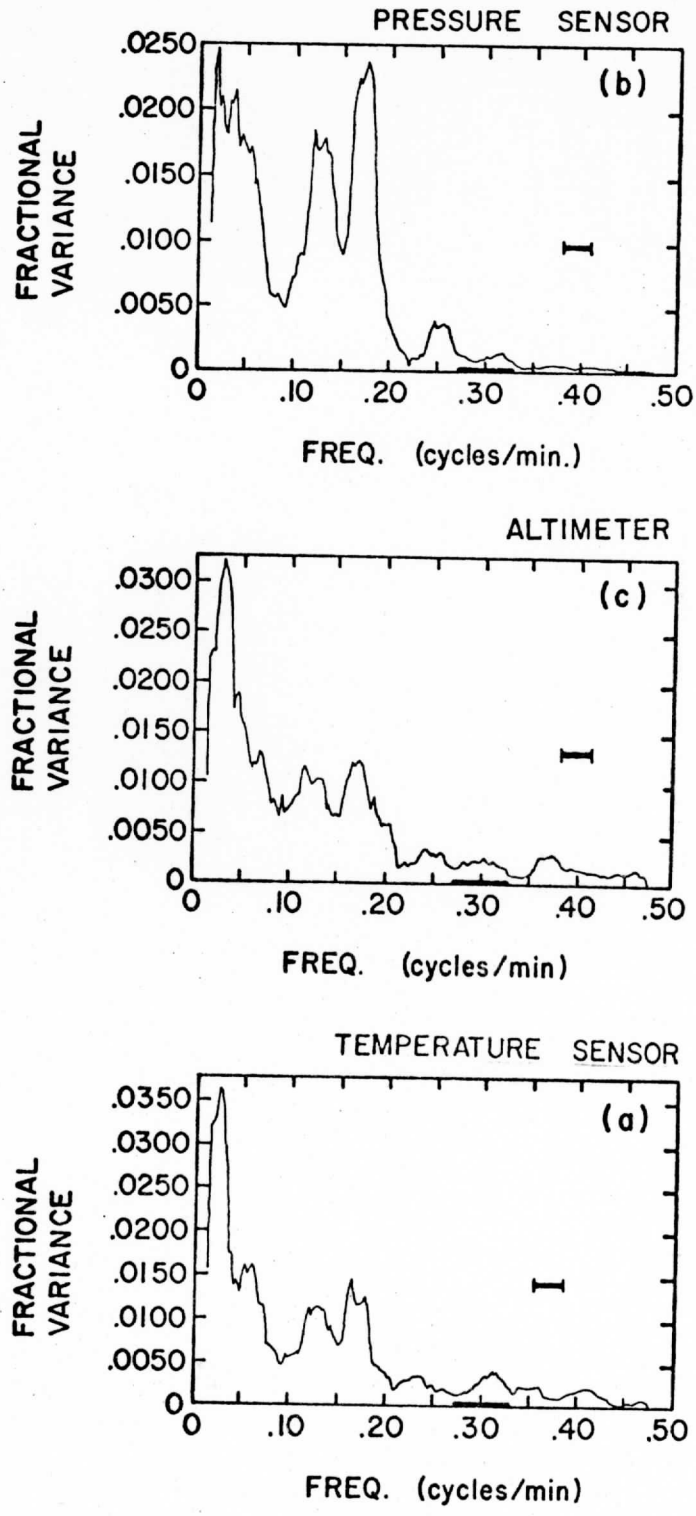

Figure 6. Variance spectra of filtered sensor data for platform 0376.

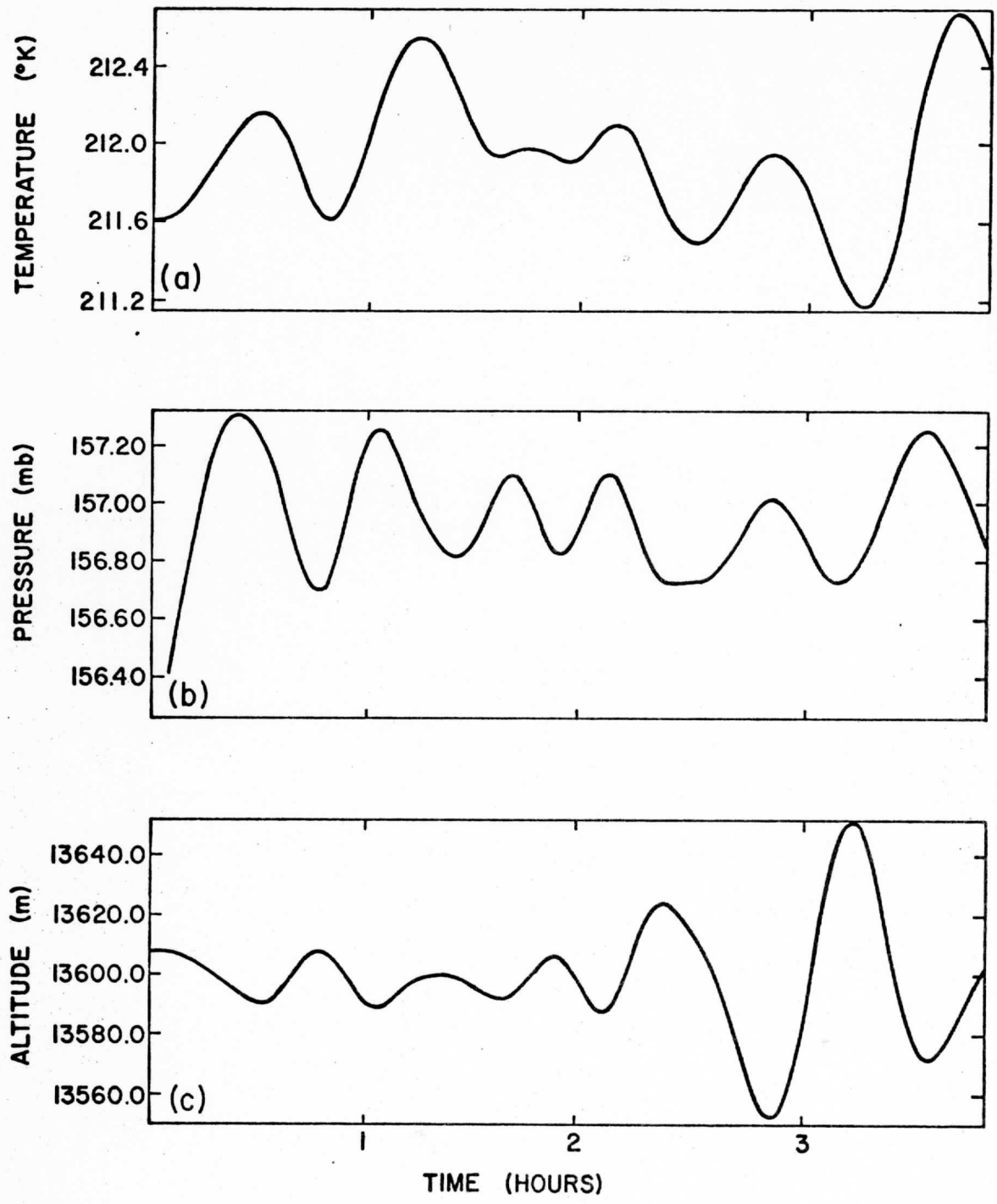

Figure 7. Filtered sensor data time series.

background pressure and the pressure oscillations due to balloon motion. In addition to helping determine the wave intrinsic frequency, the smoothing insures that all frequencies near the balloons's neutral buoyancy oscillation are filtered out before solving for w'(t). The uncertainties in both the instrument readings and the intrinsic frequency cause errors, with the latter contributing the greatest portion. By smoothing the time series, the errors in the amplitudes of w'(t) and p'(t) are reduced. The product series of these two time series is averaged over its length to find the vertical energy flux. The product series of vertical velocity, w'(t), with itself is then used to find vertical flux of horizontal momentum.

Interpretation of Results

Since the sign of the momentum flux for each individual case (except for the mountain induced waves) is uncertain, no true average value can be computed for this flux. But by assuming that the fluxes are all either positive or negative, it is possible to compute bounds on the average momentum flux. In discussing the magnitude of the momentum flux, it should be stressed that it is the value of this bound that is being used. The global set of balloon-made gravity wave observations is given in Appendix B.

Since the most obvious source for generating gravity waves is the Andes mountains, this case will be discussed first. The tropopause region, which represents a less obvious sink, will be discussed second. This region appears to be removing energy from these waves, acting as an important mechanism for the dissipation of kinetic energy at that level. Finally, it will be shown that the jet stream is a significant source for generating gravity waves and hence they may account for some of the difference between observed and computed jet stream wind speeds. The role of the jet stream will be discussed last.

A) Generation of Gravity Waves in the Andes Region

In all there are eight possible mountain lee or bow wave cases in the Andes: three in the troposphere and five in the stratosphere. All observed waves were within about 300 km of land. Table 2 lists each cases with its observed horizontal wavelength. Since these are standing waves, their wavelengths are determined by multiplying the observed balloon period of oscillation by the component of the horizontal velocity normal to the Andes. But because it is not possible to determine the exact region along the Andes that may be generating these waves, there is an uncertainty in computing the unit vector normal to the wave fronts.

The cases presented in Table 2 can be divided into two groups--those with horizontal wavelength less than 40 km, and those with wavelength greater than about 100 km. Previous observations (Alaka, 1960; Foldvik,

Table 2. Observations of mountain induced waves.

	Balloon ID	Date and Position of Observation		Horizontal Wavelength (km)	$\overline{w'}$ (cm/sec)	$\overline{p'}$ (mb)	$\overline{p'w'}$ (w/m^2)	$\overline{\rho_o u'w'}$ ($dynes/cm^2$)
Tropospheric Cases	CJ004*	Feb. 2	3S,84W	32	51	0.9	9.14	-12.6
	CJ004*	Feb. 4	1N,81W	31	37	0.8	4.83	- 8.9
	CJ007*	May 31	18S,76W	17	20	0.2	1.28	- 2.1
Stratospheric Cases	CJ002*	Dec. 12	40S,77W	253	6.9	0.4	0.38	- 0.1 (±0.1)
	CJ001*	Dec. 14	43S,77W	124	7.3	0.2	0.09	- 0.02 (±0.09)
	CJ005*	Jun 4	47S,78W	38	6.6	0.3	0.31	- 0.3
	CJ005*	Jun 5	45S,66W	21	6.2	0.2	0.08	- 0.1
	CJ006*	Feb. 21	51S,80W	98	9.2	0.3	-0.25	+ 0.07 (±0.1)

1962; Vergeiner and Lilly, 1970; Vergeiner, 1971; Lilly and Lester, 1974) show that most stationary lee waves have a horizontal wavelength of about 10 km to 25 km. This corresponds roughly with the first group.

Those observations in the second group may not be standing waves but traveling waves, such as those observed in the lee of the Rockies (Vergeiner and Lilly, 1970) with horizontal wavelengths between 40 km and 80 km. Theoretically, there is no reason that longer wavelengths cannot occur when wind shear is included. But for this study, it will be assumed that for traveling or standing waves, the magnitude (and probably direction) of the momentum flux is not much affected by wind shear. This can be seen by comparing the momentum flux for the stationary wave assumption with that for the nonstationary wave assumption, enclosed in parenthesis immediately on the right in Table 2.

The momentum flux is downward in the troposphere and in some cases quite large, but it tends to agree with other observed momentum fluxes (Bretherton, 1969; Lilly, 1972; Lilly and Lester, 1974; Hooke and Hardy, 1975). The momentum flux is much lower for the stratospheric cases, implying that much of the wave flux is "removed" in a region around the tropopause. Quantitatively the "average" energy and momentum fluxes of these waves are + 5.08 w/m^2 and - 7.9 $dynes/cm^2$ for the tropospheric waves, and + .12 w/m^2 and - 0.1 $dynes/cm^2$ for the stratospheric waves.

Somewhere in the region around the tropopause the energy flux associated with these waves is dissipated by turbulence; furthermore, the divergence of momentum flux acts as a drag force on that region of the atmosphere. The dissipation of kinetic energy due to this divergence of momentum flux is given by $-u_H \partial(\rho \overline{u'w'})/\partial Z$.

In an 18 m/sec* wind, if the momentum flux divergence occurs within a region 100 mb thick, the dissipation of kinetic energy is about 14 $w/m^2/100$ mb. This agrees with other observations of kinetic energy dissipation due to mountain induced waves (Lilly and Kennedy, 1973). Most of the convergence of the vertical energy flux probably goes into the production of available potential energy (Lindzen, 1973; Lilly, 1972), returning energy to the region in the form of turbulent energy.

Also included in Table 2 are three cases where the energy flux is downward. These could be related to partial or total reflection of a wave at some higher interface, or even to a secondary source (Eliassen and Palm, 1960) at a higher altitude quite unrelated to the Andes as assumed earlier.

B) The Role of the Tropopause as an Energy and Momentum Sink

---

*Average balloon velocity normal to the Andes.

The region around the tropopause acts as a sink for the removal of energy and momentum associated with mountain lee or bow waves. This effect of the tropopause region is also exerted on traveling waves, as can be seen by comparing all the troposperic cases with all the stratospheric cases (excluding the lee waves) listed in the tables in Appendix B. There are 59 tropospheric cases, with an average vertical energy flux per case of + 1.04 w/m^2 and a momentum flux magnitude of about 0.58 $dynes/cm^2$. There are 124 stratospheric examples, with an average vertical energy flux of + 0.37 w/m^2 and an average momentum flux magnitude of 0.24 $dynes/cm^2$.

Thus, there is a significant difference in the vertical energy flux and in the magnitude of the momentum flux between tropospheric and stratospheric averages. The convergence or divergence of momentum flux cannot strictly be determined because of the ambiguity of its sign, but the large difference in "average" magnitude strongly indicates that some convergence or divergence is taking place.

For both the traveling waves and the mountain waves, the vertical energy flux converges at a region about the tropopause. It is reasonable, therefore, to assume that the horizontal momentum flux associated with the traveling waves diverges in the tropopause in a manner similar to that of the stationary mountain waves. This divergence of the momentum flux for the traveling waves, then, could result in a drag force on a global scale comparable to the globally averaged mountain wave drag. The resulting global dissipation of kinetic energy due to these traveling gravity waves, assuming a mean wind of 30 m/s, would be $0.85 w/(m^2 - 100 mb)$, which agrees with Kung (1967, 1969) and with the results outlined in the previous chapter. When only the memory unit data are averaged together, the results and conclusions are the same; the individual values of the average fluxes change slightly but the dissipation is slightly greater--1.1 $watt/(m^2 - 100mb)$.

From the preceding data analysis, we have seen that instrumented balloons give reasonable estimate of the vertical fluxes of energy and horizontal momentum as well as the kinetic energy dissipation associated with both stationary mountain induced gravity waves and traveling gravity waves. These findings, however, are based on the assumption that, on the average, these traveling waves behave in a manner similar to their stationary counterparts with regard to the convergence of vertical energy flux and the divergence of the vertical flux of horizontal momentum.

We have also shown that, for the region around the tropopause, these gravity waves are an important mechanism for the dissipation of kinetic energy on a global scale. But it is also possible from this data set to infer another important large scale dynamical aspect of these waves (see next section).

C) Relationships Between Gravity Waves and Jet Streams

Most of the waves arriving at the tropopause have their origins below this atmospheric region. This is quite evident in Appendix B; the great majority of cases shown have upward directed vertical fluxes. As a first step in an attempt to find a generating source for these waves, all observations (except the mountain related waves) within a 5° latitude belt were averaged and presented in Table 3.

From this table we see that, in the region between about 45°S to 50°S, the maximum of both energy and momentum fluxes coincides exactly with the position of the Southern Hemisphere polar jet (Van Loon et. al 1971). The maximum between 35°S and 40°S is probably related to the seasonal or geographical variability of the polar jet. Comparisons between satellite photographs and near simultaneous gravity wave observations often show the polar jet, or the polar front, nearby. The coincidence of the maximum fluxes and the subtropical jet is not as clear, due to the fact that the position of this jet is not well known. Since the TWERLE float altitude is usually above the jet stream velocity maximums, it is clear that the jet represents a source for generating these waves. Once created, these waves then carry momentum and energy away from the jet stream; they could, therefore, represent a significant factor in the difference between observed wind maxima and the maximum winds computed by the general circulation model. This idea has been suggested earlier (Donn et al., 1973).

These waves, then, are probably as important a component in the general circulation as are the mountain induced waves for explaining this difference. The zonal average of the momentum flux associated with mountain waves is between 0.1 dynes/cm^2 and 0.4 dynes/cm^2 (Lilly, 1972) which is comparable to the "global averages" associated with the jet stream related waves of Table 3. Furthermore, the shear instability of the jet may also represent a nearly constant source of these waves, in much the same way that mountains are a constant source of lee and bow waves.

At this point in the discussion, it is worth noting one special case. On 27 June 1977, one of the memory balloons (CJ007) observed a gravity wave at 33°S, 126°W while traveling at a velocity in excess of 68 m/sec. A subsequent check of the satellite pictures for that day and region revealed a jet at exactly the same location. The observed vertical energy flux was .21 w/m^2, with an associated momentum flux of 0.1 dynes/cm^2.

One final aspect of the relationship between the jet stream and these gravity waves which is extremely important is only hinted at by this experiment. If such waves are often created by shear instability, then they may play a very important role in explaining why severe weather is so often associated with the jet stream. The waves observed in this study, thought to be jet stream related, typically have an intrinsic period between one and two hours (The special case noted

Table 3. Vertical energy and momentum fluxes for non-mountain induced waves.

Latitude Belt	$\overline{p'w'}$ Average (w/m^2)	$\overline{\pm\rho_o u'w'}$ Average ($dynes/cm^2$)	No. of Observations	Comments
5N - Eq	0.35	0.5	2	
Eq - 5S	---	---	0	
5S - 10S	0.28	0.7	8	Ascension Island first day data only
10S - 15S	1.26	0.6	10	9 American Samoa flights (first day data)
15S - 20S	0.90	0.4	4	
20S - 25S	1.85	1.0	5	
25S - 30S	1.10	0.4	16	
30S - 35S	0.12	0.2	15	
35S - 40S	0.71	0.3	18	
40S - 45S	0.37	0.3	25	13 New Zealand flights (first day data)
45S - 50S	0.61	0.3	16	
50S - 55S	-0.08	0.1	14	
55S - 60S	-0.08	0.2	9	
60S - 65S	0.02	0.2	10	
65S - 70S	0.06	0.1	4	

above had an intrinsic period of 65 minutes.) Uccellini (1975) has found evidence that a wave with a period of about 3 hours could initiate thunderstorms. Thus, gravity waves may represent an important mesoscale connection between the jet stream and severe weather. Much more study is required before such a relationship could be fully established, but data from this experiment and other balloon experiments may be one of the best approaches to such study.

Conclusions

Three major conclusions are offered in this section. First, a properly instrumented, free floating, constant density balloon is a very useful tool for globally observing gravity waves with intrinsic period between one half and three hours. Meaningful values of the vertical energy flux and the magnitude of the vertical flux of horizontal momentum associated with these waves can be determined from data gathered by such balloons.

Second, gravity waves that are generated in the troposphere and move upward appear to systematically deposit energy in a region around the tropopause. Hence, if the momentum flux is downward on the average (as it is very reasonable to expect), these waves act as a mechanism for the dissipation of kinetic energy on a global or general circulation scale.

Third, the jet stream appears to play a major role in generating these waves. Furthermore, because gravity waves transport energy and momentum away from the jet, they may be as important as mountain generated lee waves in explaining the total difference between observed and computed average jet stream wind speeds. This association with the jet stream may also indicate an important mesoscale link between gravity waves, the jet stream and severe weather.

ACKNOWLEDGEMENTS

The authors are indebted to the TWERLE team members at NCAR: P. Julian, V. Lally and W. Kellog and to C. Cote of NASA, and to E. Lichfield, N. Carlson and M. Verstraete of NCAR for launch site assistance.

This research was supported by NASA Grant NSG 5126.

APPENDIX A: Memory Balloons

Introduction

The Tropical Wind, Energy Conversion and Reference Level Experiment (TWERLE) was performed in the southern hemisphere from June 1975 to September 1976 through the cooperation of the Goddard Space Flight Center, NASA, the University of Wisconsin-Madison and the National Center for Atmospheric Research. The scientific goals of this experiment are: to measure wind and temperature in the tropical troposphere; to measure the rate of conversion of potential energy to kinetic energy; to provide a reference level for remote atmospheric temperature soundings; and to investigate atmospheric gravity waves (TWERLE Team, 1977). To achieve these objectives, over 400 instrumented constant density balloons were launched from four southern hemisphere sites during the last six months of 1975.

The analysis of data from test flights of the TWERLE system, carried out from Ascension Island in September 1974, revealed the presence of low frequency (1/2 to 3-hour period) vertical balloon oscillations which may be ascribed to atmospheric buoyancy waves similar to ocean surface waves. Investigation of these motions required periods of continuous data--a requirement that exceeded the capabilities of the original instrumentation system. To solve this problem, the original system was expanded to include onboard data averaging and storage capabilities. The storage system, (hereafter referred to as the TWERLE Storage System (TSS)) is described in detail in this appendex.

The TSS averages data over eight equally spaced samples in a nine minute interval and stores the result in a memory. Up to seven hours of these nine minute averages can be stored in this memory unit. Data in excess of this capacity can be recovered after the unit is filled because the most recent data overwrites the oldest data. During a satellite overpass, the entire contents of the memory can be transmitted in roughly three minutes. The standard TWERLE system without TSS typically transmits only 15 minutes of non-averaged data or less, depending on the length of the balloon-to-satellite contact, and hence could not be used to study gravity waves.

Because the quantity of data exceeds that which the Nimbus-6/RAMS can store for a single 69-second system cycle, the TSS transmits 16 times during each cycle. The transmissions from the TSS are made to appear as if they originate from 16 separate platforms, each with a distinct identification (ID) code and each meeting the transmission format set by the NIMBUS-6/RAMS ground station software requirements (Coates, 1975). The TWERLE data handling system recognizes 1000 distinct ID codes. Since only sixty-four of these codes were assigned to the TSS program, however, only four TSS units could be flown at any

one time.

To accommodate the increased transmission time, the altimeter acquisition interval was reduced to 20 seconds and the temperature and pressure sensor sampling times were reduced by a factor of two. Figure A.1 allows the comparison of the operating cycles of the standard and TSS systems.

The TSS incorporates all of the timing functions of the TWERLE data encoder, and also performs data collection, averaging and storage tasks. Data averaging is necessary to avoid aliasing high frequency natural balloon oscillations, and data storage is necessary to allow for much longer data samples. The block diagram in Figure A.2 gives an overview of the functions of the TSS.

The system timing is derived from a 12.8 kHz crystal oscillator which is divided in a binary counter chain and gated to produce all external and internal timing signals. Altitude, pressure and temperature are measured by sensors whose outputs are frequencies.

The data averager counts the sensor frequencies and forms averages over eight consecutive frequency samples. The averaged data is stored in a random access memory (RAM). Chronological order of the data is maintained by defining an initial storage location at the start of the day and maintaining consecutive storage thereafter.

The SYNC-ID generation block creates a fixed-pattern preamble to each transmitted data segment and provides the segment with a valid TWERLE balloon identification code. The output multiplexer combines the synchronization and identification signals with the data, and converts the logic voltage levels to those required for transmitter modulation.

The power control block is an auxiliary unit whose function is vital to the overall data collection process. The power unit initiates data collection when sufficient solar panel power is available (after sunrise) to allow proper operation of all sensors and logic circuitry. The power unit also saves the memory contents by switching to auxiliary battery power at night and during temporary solar panel dropouts.

Although many of the functions of the TSS are similar to those of the encoder used in the standard TWERLE instrumentation platform, some TSS capabilities--data averaging, storage and power turn on and memory save--are added features (described below).

Data Averager

The data averager computes the average of eight consecutive samples of each of four different sensor frequencies. It consists of a counter,

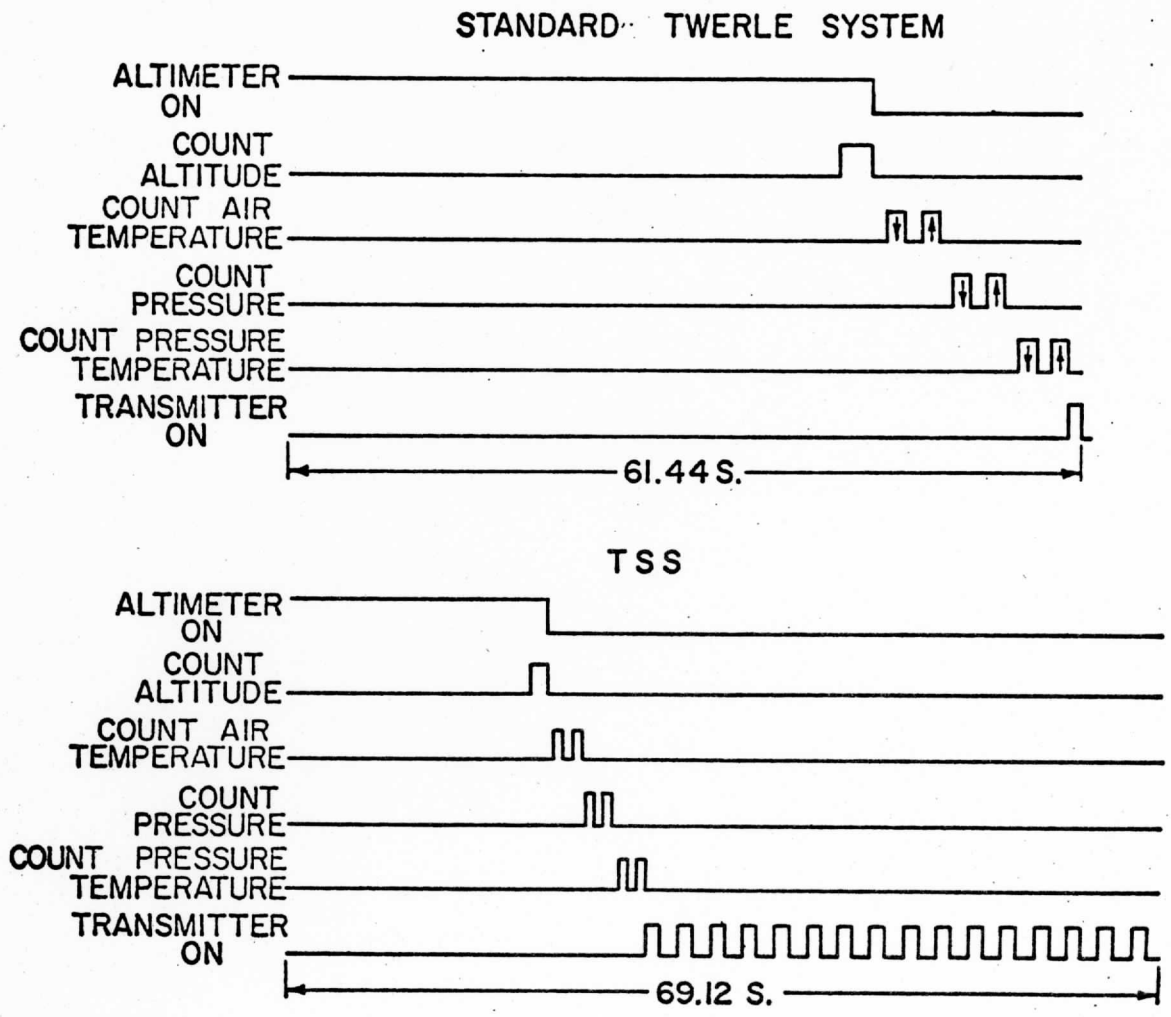

Figure A-1. Timing diagram.

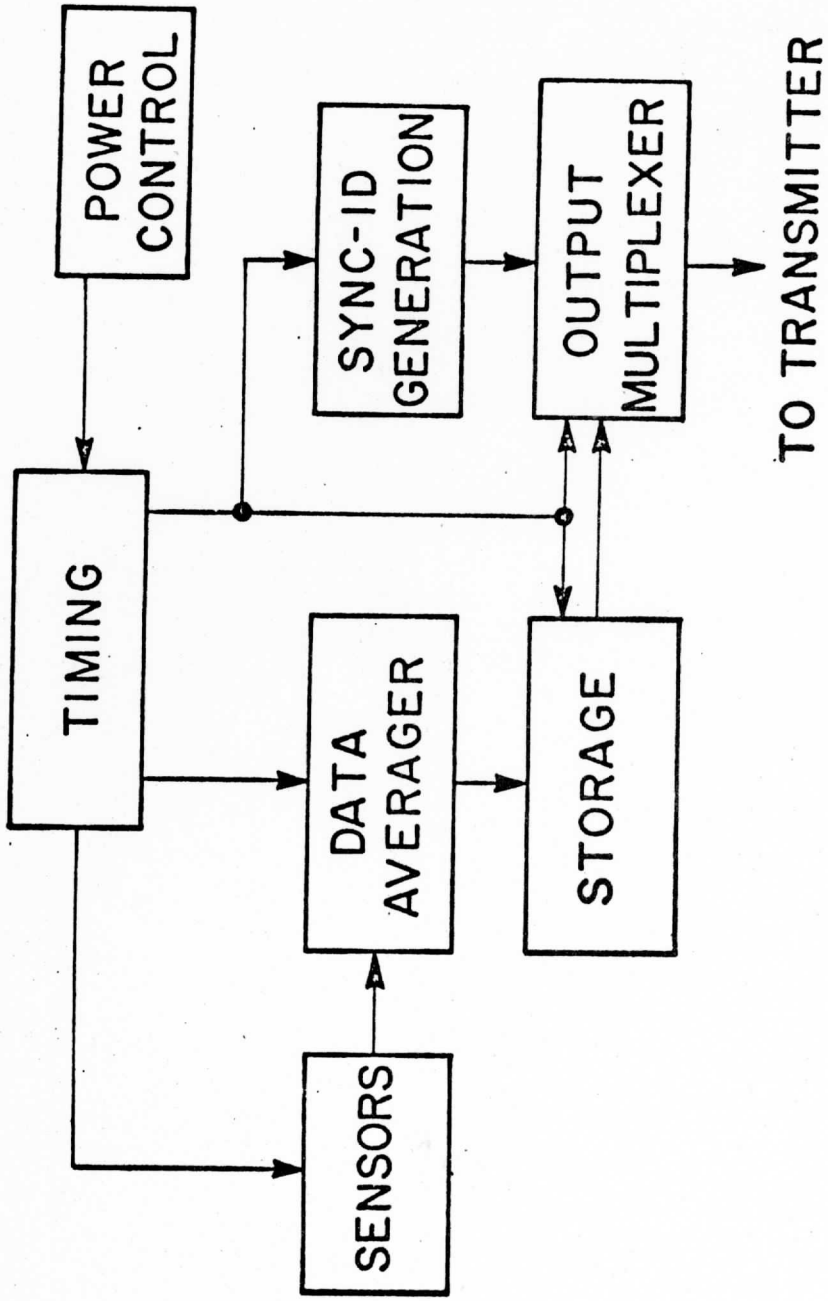

Figure A-2. TSS functional block diagram.

a multi-functional data register and a shift register. The average is accumulated in the counter, transported in and out of storage through the data register, and stored temporarily in both the shift register and the data register. The interconnections between components and data flow in the averager are given in Figure A-3.

In operation, a particular sensor frequency is counted, stored temporarily in the shift register, pre-set into the counter, counted on top of, or stored in the shift register. This procedure terminates when the total count corresponds to the sum of eight consecutive frequency samples from the sensor. Division by 8 is accomplished by using counter bits which are shifted three bits to the most significant bit (MSB) side. The averaging procedure carries 12 bits to maintain accuracy. When the averaged data is shifted into the memory only the eight MSB's of each sensor count are used.

There is a truncation error in this averaging scheme. Each time that a number transferred from the counter to temporary storage, the three least significant bits (LSB's) are truncated and dropped. Since this process is carried out eight times, the six LSB's of the 16-bit counter are affected. When transferred to the 12-bit shift register section, the three LSB's are affected. Only the eight MSB's are transferred to storage, so the truncation error is of no consequence.

In actual use, the averaging procedure is more complicated for three of the four sensors. For these sensors a reference frequency is counted down before the sensor frequency is counted up. Averaging is then performed on the resultant difference of two counts.

Storage Circuitry

The storage circuitry is comprised of a 1536-bit C-MOS memory (made up of three 512-bit chips; AMI S2222) with its associated cycle generator and read/write address counters. The memory is organized into a 48-row by 32-column array. Each 32-bit row contains a data segment consisting of four 8-bit sensor data words, and each memory operation, whether read or write, manipulates a complete segment. Segments are selected via the read and write address counters. One segment is stored into the memory every eight system cycle times (9.2 minutes) at a 400 bps rate; output from the memory is 16 segments per cycle at a 100 bps rate. Thus, the entire contents of the memory, 48 segments, are output in three system cycles.

A block diagram of the storage circuitry is shown in Figure A.4. The memory cycle generator executes a complete cycle for each and every bit that is written into or read out of the memory. During such a cycle the memory control signals, READ/WRITE ENABLE and CHIP ENABLE and DATA OUTPUT STROBE are generated with proper timing with respect to the start of the memory cycle as well as with respect to each other. The column address counter sweeps out an entire row (segment) with each read or

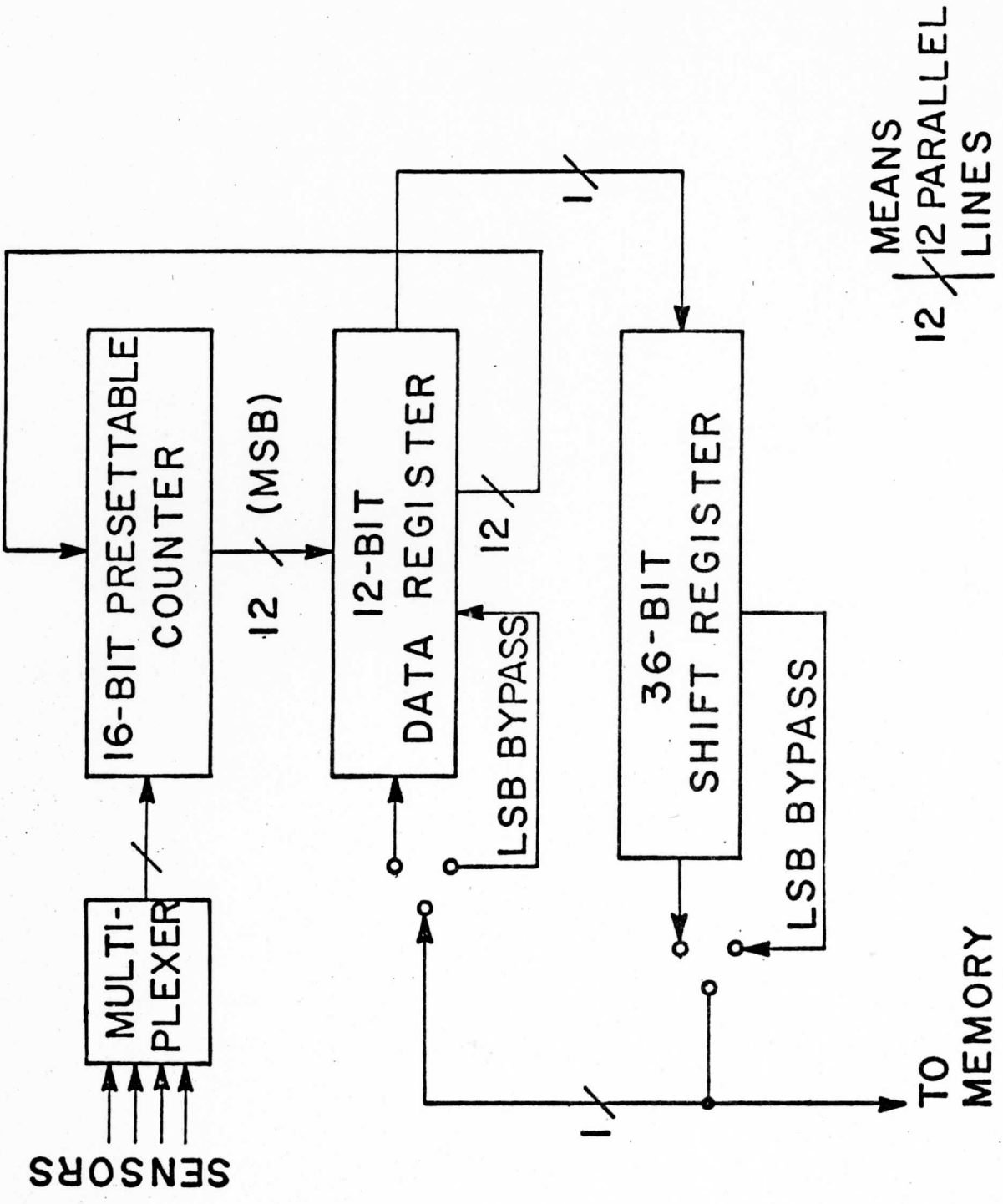

Figure A-3. Data averager block diagram.

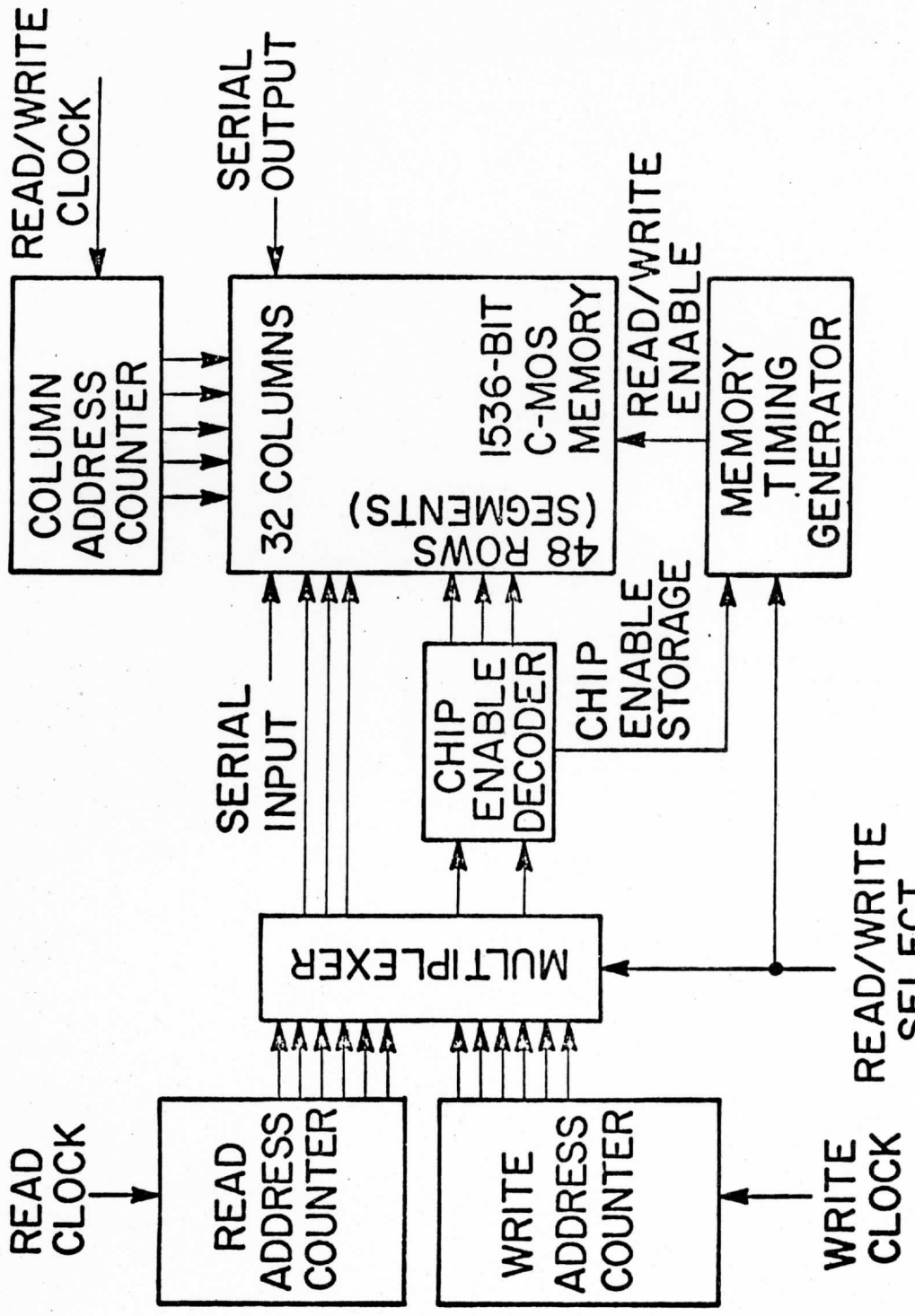

Figure A-4. Storage circuitry.

write operation; thus, data is always handled in complete segments. The read and write address counters select the particular segments to be processed and provide storage for the location of the most recent transaction. The multiplexer selects between the read and write addresses. The chip enable decoder uses the most significant address bits in conjunction with the chip enable strobe to select the proper 512-bit chip. Data is latched at both the input and output of the memory to maintain synchronization with the read and write operations.

Power Unit

The power unit provides a start signal for the collection of data after sunrise. The instrumentation platform is solar panel powered, so data collection and subsequent averaging and storage must not begin until adequate solar power is available for correct sensor and processing circuit operation. The proper starting point is selected by sampling solar panel power via heater resistors mounted inside a miniature Dewar flask. This heater/flask arrangement integrates the power fluctuations of the solar panel at the start of the day. When the Dewar temperature reaches the tripping point of a thermal switch in the Dewar flask, the data collection procedure is initiated. At night, the Dewar cools off and the thermal switch releases.

The power unit also must preserve the contents of the volatile C-MOS memory during power dropouts and transients. When the sun is at a very high angle--for example, when the balloons drift toward the equator--there is a possibility that the solar panel may be in the shadow of the balloon and the 401.2 MHz antenna. If, in addition, there is some pendulum oscillation of the flight train, there will be fluctuations in solar panel power as the panel swings in and out of the balloon/antenna shadow.

Figure A.5 is a block diagram of the power unit. The +12 V from the solar panel power bus is shunt regulated to +6.8 volts and fed to the thermal switch through an isolating diode. A battery is coupled to the thermal switch through a second diode, and if the solar panel power drops out, the diode network automatically applies battery power. The voltage level available from the solar panel is sampled continuously. If the level drops below that required for proper meteorological sensor operation, a system reset is generated to stop further data collection and to put the memory into a save state. When solar panel voltage is restored, the memory contents at the point of power failure are marked with a segment of all 0's; then data collection resumes.

Packaging and Physical Considerations

All TWERLE flight train components are fabricated to be light weight to minimize balloon load and to minimize mass in case of collision with an aircraft. The TSS is fabricated with these considerations in

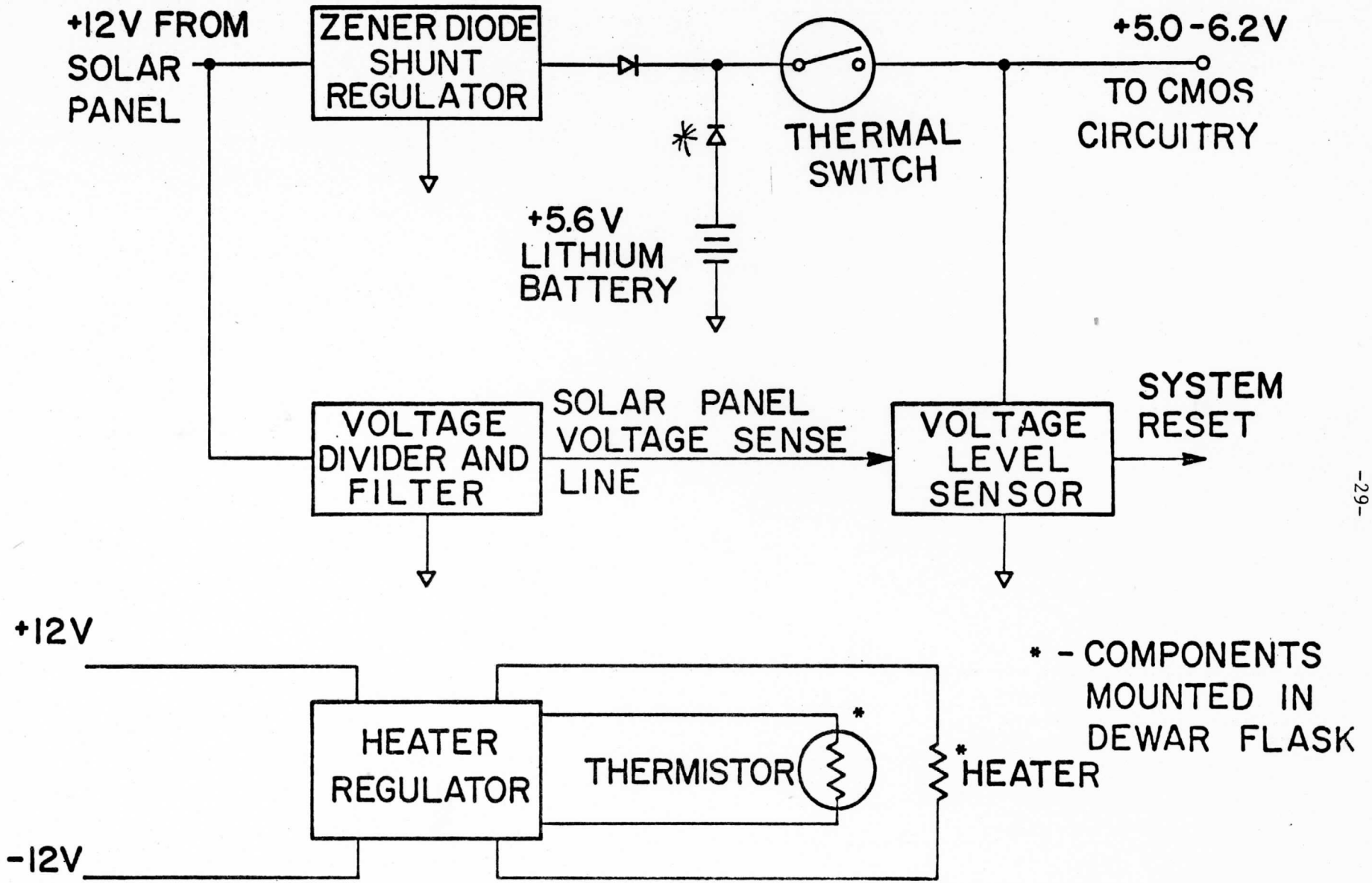

Figure A-5. Power unit block diagram.

mind. The circuitry is contained on two 8 x 10 inch, .006 thick fiber glass boards. The boards are curved around the inside walls of a cylindrical styrofoam package which provides physical as well as thermal protection. The Dewar flask and the power circuitry are mounted in a styrofoam block on the bottom of the package. A sketch of the TSS is presented in Figure A.6.

The cylindrical package can be fabricated easily. Styrofoam behaves well under compression but tolerates very little tension before breaking, but if a non-stretching material such as paper, mylar, or aluminum foil is bonded to a sheet of styrofoam, the properties of the sheet are markedly altered. The sheet can now be bent to a small radius as long as the reinforced surface is kept to the outside of the curve.

The package for the TSS was constructed of 1/2 inch styrofoam using Scotch No. 467 transfer adhesive to bond aluminum foil to the outer side of the sheet. The resultant package is tough and flexible and springs back to the cylindrical shape even after gross distortion.

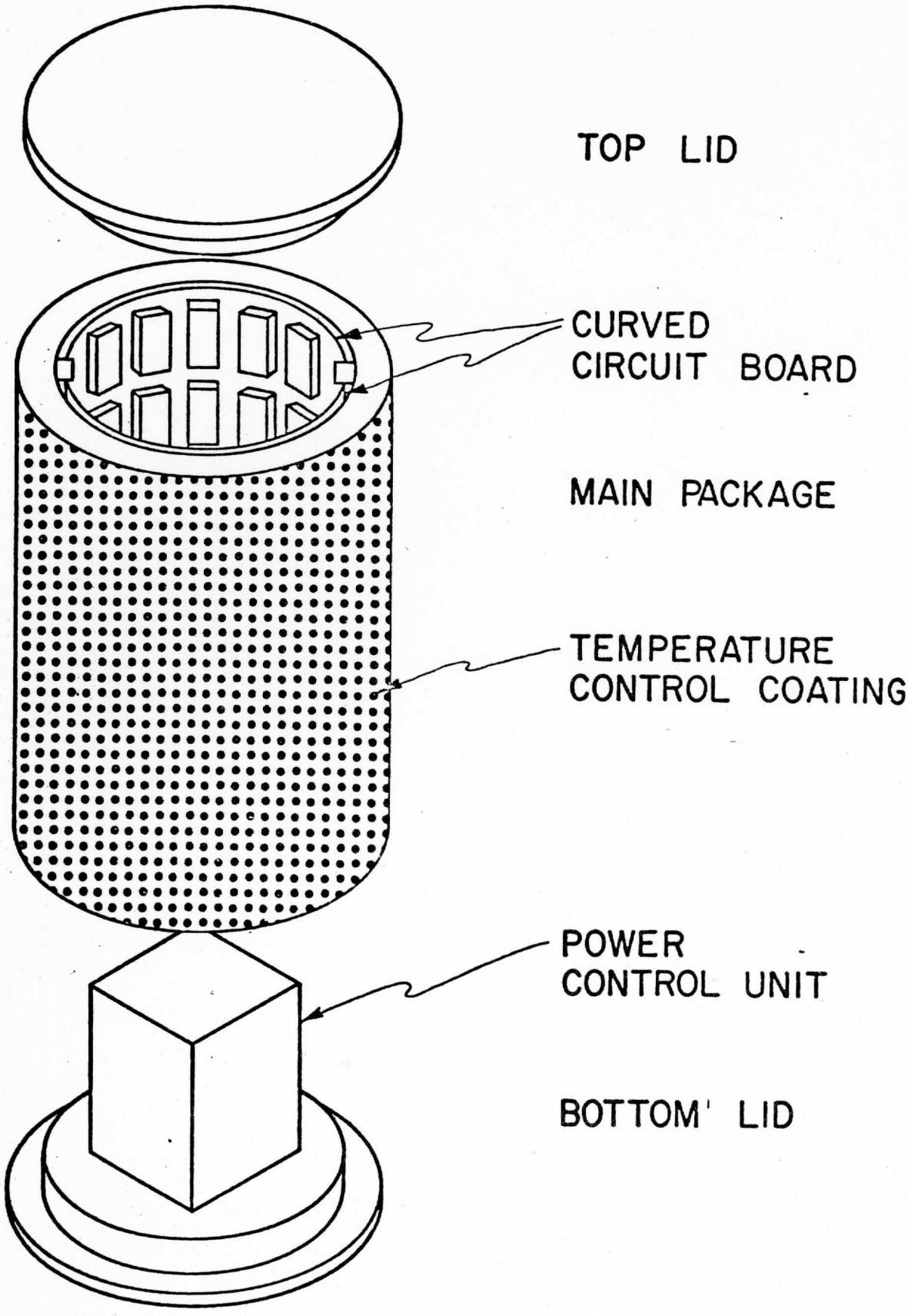

Figure A-6. TSS Package

APPENDIX B: Individual Gravity Wave Observations

This appendix tabulates the total number of gravity wave observations from both the first-day data set and the memory unit data set. The directions of all momentum fluxes are unknown except for the eight mountain wave cases. When "average flux" values are computed, it is assumed that these fluxes are negative and therefore act as a drag force on the atmosphere.

Table B.1, which lists the gravity wave observations from the first day data set, suggests several tentative conclusions. Of the 18 tropical cases, 15 have positive vertical energy fluxes and 3 have negative values. If the tropical launch sites are typical of the hemispheric upper troposphere, this indicates that the lower troposphere is a strong source of these waves with very little reflection occurring at this level. Based on these observations, an "average" upper tropospheric internal gravity wave at TWERLE level would have an upward vertical energy flux of about 0.47 w/m^2.

In contrast, however, 5 of the 13 midlatitude observations (all from the same launch station) have negative vertical fluxes of energy, which would indicate either reflection or creation of these waves at a region above the tropopause. If this station is representative of the hemispheric lower stratosphere, then the "average" vertical energy flux for a wave in this region would be about 0.02 w/m^2. Again the flux is upward but with a significantly smaller magnitude than in the tropospheric cases. In some "quasi-vertical" sense (comparing the tropical tropospheric and midlatitude strato-spheric observations), there is evidence that these waves are generating available potential energy within a region around the tropopause by the convergence of the vertical energy flux.

The momentum flux, like the energy flux, also shows a difference in magnitude across the tropopause. For the average tropospheric case, the vertical flux of horizontal momentum is .6 dynes/cm^2; in the stratospheric case, the value is .3 dynes/cm^2. This difference may not be too important, but it does imply divergence of momentum flux at the tropopause region if the momentum flux is downward in some "global average" sense. This will be demonstrated more clearly with the memory unit data.

In addition to information on the large scale dynamical aspects of gravity waves, Table B-1 contains another interesting observation. On 24 August 1975, balloons 0473 and 0267 both show evidence of a wave with a 27 minute period. The magnitude of vertical energy fluxes for those two cases were very nearly the same, but opposite in direction. This is evidence for a trapped or reflected wave.

It must be stressed that these tentative deductions inferred from

the first day data set only hint at the role played by gravity waves. To verify these conclusions, observations should be taken globally at several levels throughout the atmosphere. Tables B-2 and B-3 give the results for the tropospheric and stratospheric observations, respectively. Those observations which utilized the climatological lapse rate are noted with an asterisk; they comprise about 80% of the total set of observations. The observations marked with a dagger are thought to be stationary lee waves or bow waves generated by the Andes. To determine whether the balloons were in the stratosphere or troposphere, balloon height was compared either to the soundings (when it included the tropopause heights) or to the climatological height of the tropopause (Crutcher, et al., 1971). In the region between 20°S and 35°S it was difficult to tell whether the balloons were in the troposphere or stratosphere; in other case, the decision was relatively easy.

Table B-1. Gravity Wave Observations from the First Day Data Set

	Balloon ID	Date and Station of Observation	Intrinsic Frequency (cycles/min)	Instrinsic Period (min)	Average Amplitude Vertical Velocity (cm/sec)	Average Amplitude Pressure, p' (mb)	$\overline{p'w'}$ (w/m^2)	$\overline{\pm\rho_o u'w'}$ ($dynes/cm^2$)
Tropical Launches (Below Tropopause)		Ascension Island (8S, 14W)						
	1400	July 4 (1975)	.031	32	41	0.2	0.08	0.8
	0720	July 7	.029	34	44	0.5	1.48	0.9
	0364	July 9	.016	60	16	0.2	0.23	0.2
	0546	July 10	.032	31	24	0.2	0.91	0.3
	0570	July 10	.022	44	17	0.2	0.05	0.2
	0766	August 9	.031	32	20	0.2	-0.38	0.2
	0473	August 25	.035	28	56	0.2	2.44	1.1
	0267	August 25	.037	26	81	0.3	-2.56	2.0
		American Samoa (14S, 170W)						
	1101	July 1	.018	54	25	0.3	0.43	0.4
	0104	July 20	.014	68	8	0.1	-0.02	0.1
	0754	Aug. 28	.024	41	19	0.1	0.38	0.2
	0762	Aug. 28	.025	39	26	0.2	0.38	0.4
	1135	Sept. 1	.030	33	33	0.4	2.04	0.5
	1274	Sept. 1	.028	35	28	0.3	0.96	0.4
	1765	Sept. 18	.026	38	37	0.3	0.12	0.7
	0550	Sept. 18	.015	64	29	0.3	1.39	0.8
	1240	Sept. 26	.027	36	23	0.2	0.36	0.3
		Accra, Ghana (5N, 0W)						
	0671	Aug. 12	.032	30	36	0.4	0.18	0.6

Table B-1. (Continued)

	Balloon ID	Date and Station of Observation	Intrinsic Frequency (cycles/min)	Intrinsic Period (min)	Average Amplitude Vertical Velocity (cm/sec)	Average Amplitude Pressure, p' (mb)	$\overline{p'w'}$ (w/m^2)	$\overline{\pm\rho_o u'w'}$ ($dynes/cm^2$)
		Christchurch, New Zealand (44S, 173E)						
Midlatitude Launches (Above Tropopause)	0322	Sept. 30	.018	54	7	0.1	0.07	0.1
	0024	Oct. 6	.019	51	6	0.3	0.12	0.1
	1141	Oct. 12	.019	51	12	0.1	-0.13	0.1
	1177	Oct. 12	.022	44	15	0.2	-0.25	0.2
	1712	Oct. 30	.020	49	16	0.4	1.00	0.3
	0376	Nov. 21	.026	38	22	0.6	-0.15	0.5
	0603	Dec. 8	.019	51	8	0.1	0.08	0.1
	0646	Jan. 2 (1976)	.031	33	16	0.1	0.02	0.2
	1465	Jan. 5	.026	38	15	0.2	0.32	0.2
	0727	Jan. 11	.026	39	11	0.2	0.02	0.1
	1255	Jan. 11	.030	34	18	0.3	0.02	0.3
	1201	Jan. 31	.013	73	6	0.1	-0.02	0.1
	1177	Mar. 9	.031	32	59	1.1	-0.82	2.0

Table B-2. Tropospheric Memory Unit Balloon Observations

Balloon ID	Date and Position of Observation		Intrinsic Frequency (cycles/min)	Intrinsic Period (min)	Average Amplitude Vertical Velocity (cm/sec)	Average Amplitude Pressure, p' (mb)	$\overline{p'w'}$ (w/m^2)	$\pm\overline{\rho_o u'w'}$ ($dynes/cm^2$)
CJ004*†	Feb 2	3S,84W	0.014†	74†	51	0.9	9.14	-12.6†
CJ004*†	Feb 4	1N,81W	0.011†	95†	37	0.8	4.83	- 8.9†
CJ007*	July 25	2N,46W	0.013	78	19	0.3	0.5	0.4
CJ004*	Jan 30	11S,150W	0.014	74	50	0.9	6.58	2.5
CJ001*	Dec 12	19S,97W	0.014	71	19	0.3	0.99	0.4
CJ002	Dec 22	19S,139W	0.013	79	14	0.4	1.00	0.3
CJ007*†	May 31	18S,76W	0.021†	47†	20	0.2	1.28†	- 2.1†
CJ007	July 19	17S,130W	0.011	91	24	0.3	0.77	0.7
CJ007*	July 20	17S,87W	0.018	55	9.9	0.2	0.85	0.09
CJ002*	Dec 26	24S,106W	0.017	61	24	0.5	3.24	0.6
CJ002*	Jan 7	21S,66E	0.018	55	53	1.2	6.17	2.3
CJ008	Mar 19	21S,146W	0.013	78	35	0.7	-0.44	1.9
CJ007	May 28	24S,139W	0.16	62	8.0	0.2	0.27	0.06
CJ007*	Aug 3	23S,54E	0.0081	123	7.6	1.3	0.02	0.1
CJ007*	Dec 31	27S,95W	0.013	76	5.2	0.2	-0.03	0.04
CJ002	Jan 11	26S,160E	0.0079	126	33	1.3	2.45	2.3
CJ004*	Jan 16	26S,40E	0.012	85	31	1.1	3.40	1.2
CJ005	May 12	28S,38E	0.023	43	23	0.5	-0.16	0.4
CJ007*	June 26/27	25S,173W	0.018	55	5.8	0.2	0.22	0.03
CJ007*	July 10	25S,29W	0.015	65	15	0.3	1.68	0.3
CJ007	July 13	27S,37E	0.022	45	11	0.3	0.08	0.1
CJ005	May 16	31S,144W	0.013	78	28	0.2	0.17	0.7

Table B-3. Stratospheric Memory Unit Balloon Observations

Balloon ID	Date and Position of Observation		Intrinsic Frequency (cycles/min)	Intrinsic Period (min)	Average Amplitude Vertical Velocity (cm/sec)	Average Amplitude Pressure, p' (mb)	$\overline{p'w'}$ (w/m^2)	$\pm\overline{\rho_o u'w'}$ ($dynes/cm^2$)
CJ002	Dec 18	29.9S,114E	0.011	89	8.4	0.3	0.41	0.1
CJ002*	Dec 21	29S,128W	0.010	97	22	0.7	4.00	0.9
CJ007*	May 20	27S,8W	0.016	63	9.4	0.3	0.62	0.1
CJ007	May 21	29S,11E	0.015	68	11	0.3	0.69	0.1
CJ007*	Jun 7	27S,75E	0.017	58	6.9	0.2	0.16	0.05
CJ007*	Jun 8	26S,101E	0.023	43	7.2	0.2	0.56	0.04
CJ007*	Jun 30	29S,35W	0.018	55	9.6	0.2	0.25	0.1
CJ007	Jul 5	27S, 161E	0.011	91	11	0.2	0.55	0.2
CJ007*	Jul 6	27S,156W	0.0083	120	20	0.6	3.64	0.9
CJ001*	Dec 4	34S,174W	0.0091	110	7.3	0.2	0.18	0.1
CJ002*	Dec 8	34S,171W	0.014	73	8.4	0.2	-0.01	0.1
CJ007*	Feb 22	34S,115W	0.012	83	6.8	0.2	0.22	0.08
CJ008*	Mar 11	33S,165W	0.019	53	11	0.3	0.76	0.1
CJ008*	Mar 25	31S,44W	0.015	66	13	0.2	0.27	0.2
CJ007*	Apr 24	32S,41W	0.014	74	11	0.1	-0.07	0.2
CJ005*	May 13	30S,71E	0.012	85	7.2	0.2	0.54	0.09
CJ007	May 13/14	33S,167E	0.020	51	9.3	0.3	0.22	0.09
CJ007*	May 23	30S,65E	0.014	74	9.2	0.2	-0.18	0.1
CJ007*	Jun 24	32S,86E	0.014	74	13	0.1	-0.29	0.3
CJ007	Jun 26	34S,154E	0.010	101	10	0.2	-0.62	0.2
CJ007*	Jun 27	33S,126W	0.015	65	8.5	0.3	0.21	0.1
CJ007*	Jun 28	30S,90W	0.015	68	9.2	0.2	0.09	0.1
CJ007*	Jul 15	30S,88E	0.017	61	7.6	0.2	0.25	0.07

Table B-3. (Continued)

Balloon ID	Date and Position of Observation		Intrinsic Frequency (cycles/min)	Intrinsic Period (min)	Average Amplitude Vertical Velocity (cm/sec)	Average Amplitude Pressure, p' (mb)	$\overline{p'w'}$ (w/m^2)	$\pm\overline{\rho_o u'w'}$ ($dynes/cm^2$)
CJ002*	Dec 10	39S,142W	0.011	92	7.6	0.4	0.05	0.1
CJ002*	Dec 17	36S,106E	0.0095	105	5.9	0.2	0.16	0.08
CJ002*	Dec 27	38S,92W	0.013	76	12	0.4	0.34	0.2
CJ004*	Jan 17	39S,69E	0.0090	111	23	1.8	2.00	1.3
CJ004	Jan 26	38S,155E	0.014	72	18	1.2	3.54	0.5
CJ004*	Jan 28/29	35S,131E	0.013	76	21	1.0	3.84	0.7
CJ006	Feb 17	37S,170E	0.011	92	7.8	0.4	0.15	0.1
CJ007*	Feb 20	38S,148W	0.019	53	6.1	0.2	0.40	0.04
CJ006*	Feb 27	38S,9E	0.019	52	13	0.5	0.83	0.2
CJ008*	Mar 30	39S,97E	0.013	80	8.2	0.2	0.36	0.1
CJ007*	Apr 7	37S,152E	0.017	58	14	0.5	1.08	0.2
CJ007*	Apr 27	37S,64E	0.0090	111	11	0.5	-0.11	0.3
CJ005*	May 14	35S,90E	0.016	63	8.6	0.4	0.10	0.1
CJ005*	May 17	38S,110W	0.017	59	6.6	0.2	-0.17	0.06
CJ005*	May 24	39S,23W	0.011	88	3.8	0.1	-0.08	0.03
CJ005*	May 25	39S,3E	0.017	59	10	0.2	-0.03	0.2
CJ005*	Jun 16	39S,156W	0.014	74	13	0.4	0.43	0.3
CJ007*	Jul 1	36S,1W	0.014	74	7.6	0.3	-0.03	0.1
CJ002*†	Dec 12	40S,77W	0.0090†	111†	6.9	0.4	0.38	-0.1†
CJ001*†	Dec 14	43S,77W	0.020†	50†	7.3	0.2	0.09	-0.02†
CJ002*	Dec 14	43S,13E	0.0096	104	8.7	0.2	-0.03	0.2
CJ004*	Jan 12	44S,91W	0.010	97	20	1.5	1.60	1.0
CJ004*	Jan 14	41S,25W	0.0097	103	19	1.2	0.31	0.8

Table B-3. (Continued)

Balloon ID	Date and Position of Observation		Intrinsic Frequency (cycles/min)	Intrinsic Period (min)	Average Amplitude Vertical Velocity (cm/sec)	Average Amplitude Pressure, p' (mb)	$\overline{p'w'}$ (w/m^2)	$\pm\overline{\rho_o u'w'}$ ($dynes/cm^2$)
CJ008	Apr 1	40S,176W	0.025	40	31	0.8	6.60	0.8
CJ007*	Apr 2	42S,34E	0.0094	107	6.8	0.3	0.11	0.1
CJ007*	Apr 3	44S,66E	0.010	96	11	0.2	-0.33	0.3
CJ007*	Apr 7	40S,160E	0.019	54	14	0.7	0.52	0.2
CJ007*	Apr 9	43S,137W	0.011	89	4.6	0.2	-0.02	0.05
CJ007*	May 11	41S,123E	0.014	74	6.8	0.3	0.12	0.08
CJ005*	May 28	43S,103E	0.0094	106	16	0.8	0.25	0.7
CJ005*	Jun 12	43S,109E	0.026	36	8.8	0.1	0.08	0.08
CJ005	Aug 2	43S,14W	0.019	52	8.5	0.2	-0.36	0.1
CJ002*	Dec 15	47S,56E	0.0056	179	16	0.1	1.91	1.1
CJ004*	Dec 30	48S,12E	0.0097	103	8.4	0.5	0.29	0.2
CJ004*	Jan 13	47S,60W	0.011	89	24	1.9	4.08	1.3
CJ004	Jan 25	45S,146E	0.0090	111	14	1.1	1.55	0.5
CJ006*	Feb 20	46S,100W	0.017	58	19	0.9	1.90	0.5
CJ007	Feb 27	49S,40E	0.0082	122	5.7	0.3	-0.13	0.1
CJ008*	Mar 26	45S,13W	0.016	61	4.0	0.1	0.00	0.02
CJ007*	Apr 12	45S,58W	0.010	96	7.3	0.3	-0.33	0.1
CJ007*	Apr 14	49S,6E	0.015	67	6.6	0.2	-0.16	0.07
CJ007*	Apr 15	46S,39E	0.014	74	7.8	0.2	0.28	0.1
CJ007*	Apr 21	45S,110W	0.014	71	7.1	0.4	0.32	0.09
CJ007*	May 6	45S,25W	0.021	47	9.0	0.3	-0.43	0.1
CJ007	May 8	47S,48E	0.018	55	7.3	0.3	-0.08	0.09
CJ005*†	Jun 4	47S,78W	0.014†	69†	6.6	0.3	0.31	-0.3†

Table B-3. (Continued)

Balloon ID	Date and Position of Observation		Intrinsic Frequency (cycles/min)	Intrinsic Period (min)	Average Amplitude Vertical Velocity (cm/sec)	Average Amplitude Pressure, p' (mb)	$\overline{p'w'}$ (w/m^2)	$\overline{\pm \rho_o u'w'}$ ($dynes/cm^2$)
CJ005*†	Jun 5	45S,66W	0.017†	59†	6.2	0.2	0.08	-0.1†
CJ005*	Jul 1	45S,19W	0.012	85	7.5	0.2	0.04	0.1
CJ005*	Jul 25	49S,10E	0.012	82	8.6	0.3	0.20	0.2
CJ005*	Jul 26	48S,43E	0.014	71	14	0.1	0.35	0.4
CJ003*	Dec 11	55S,168W	0.0066	151	4.4	0.2	0.09	0.08
CJ004*	Dec 31	51S,35E	0.0062	162	6.4	0.3	-0.23	0.2
CJ004*	Jan 5	51S,125E	0.011	94	8.2	0.6	-0.03	0.2
CJ004*	Jan 8	50S,149W	0.0081	123	8.6	0.4	-0.43	0.2
CJ006*†	Feb 21	51S,80W	0.021†	47†	9.2	0.3	-0.25	0.07†
CJ007*	Mar 11	54S,81E	0.0080	124	5.7	0.2	0.02	0.1
CJ007*	Mar 13	53S,120E	0.015	68	7.9	0.2	-0.11	0.1
CJ008*	Mar 31	52S,139E	0.013	80	5.7	0.4	-0.44	0.07
CJ007*	Apr 4	53S,117E	0.013	77	9.5	0.4	0.57	0.2
CJ007*	Apr 8	50S,173W	0.015	65	5.9	0.2	0.09	0.06
CJ007*	Apr 17	50S,99E	0.0086	117	13	0.3	0.08	0.5
CJ007*	Apr 28	51S,95E	0.015	65	6.0	0.1	-0.01	0.06
CJ007	May 1/2	53S,179E	0.013	78	7.4	0.2	-0.15	0.1
CJ005*	Jun 8	50S,11E	0.022	45	7.7	0.4	-0.38	0.07
CJ005*	Jul 19	51S,67E	0.015	66	8.4	0.2	-0.15	0.1
CJ004*	Dec 19	56S,41W	0.0094	106	8.6	0.9	-0.87	0.2
CJ004*	Dec 29	57S,7W	0.012	84	6.4	0.3	-0.16	0.09
CJ004*	Jan 19	58S,112E	0.0099	101	23	2.0	0.58	1.4

Table B-3. (Continued)

Balloon ID	Date and Position of Observation		Intrinsic Frequency (cycles/min)	Intrinsic Period (min)	Average Amplitude Vertical Velocity (cm/sec)	Average Amplitude Pressure, p' (mb)	$\overline{p'w'}$ (w/m^2)	$\pm\overline{\rho_o u'w'}$ ($dynes/cm^2$)
CJ007	Mar 5	59S,66W	0.012	87	4.9	0.2	0.04	0.05
CJ007*	Mar 9	57S,34E	0.014	74	5.4	0.3	-0.33	0.05
CJ007*	Mar 10	58S,62E	0.013	77	6.2	0.2	0.16	0.08
CJ007*	Mar 14	58S,165E	0.011	92	5.2	0.3	0.07	0.06
CJ007*	Mar 22	57S,12E	0.015	68	6.6	0.3	0.11	0.07
CJ005*	Jun 26	56S,171W	0.018	55	11	0.3	-0.29	0.2
CJ004	Dec 24	63S,53W	0.0059	169	5.8	0.4	-0.14	0.1
CJ004	Dec 25	63S,47W	0.020	49	17	0.9	0.59	0.3
CJ004	Jan 3	64S,75E	0.0043	232	13	1.0	0.26	1.0
CJ004*	Jan 20	62S,119E	0.0056	177	4.3	0.3	0.03	0.09
CJ004*	Jan 21	63S,124E	0.0076	132	3.3	0.2	0.07	0.04
CJ004*	Jan 22	62S,133E	0.0078	129	5.5	0.3	-0.12	0.1
CJ007*	Mar 2	64S,175W	0.014	74	7.2	0.4	-0.17	0.1
CJ007*	Mar 7	61S,26W	0.0095	105	6.3	0.3	-0.27	0.1
CJ007*	Mar 16	61S,140W	0.014	71	6.7	0.2	0.15	0.08
CJ007*	Mar 27	62S,96W	0.014	74	8.5	0.3	-0.22	0.1
CJ003*	Dec 12	65S,151W	0.0059	170	3.6	0.3	0.01	0.06
CJ003*	Dec 13	65S,125W	0.010	98	4.1	0.2	0.05	0.04
CJ007*	Mar 3	67S,134W	0.014	71	6.5	0.3	0.02	0.08
CJ007*	Mar 21	67S,27W	0.015	68	5.9	0.4	0.14	0.06

REFERENCES

Alaka, M. A., Ed., 1960: The Airflow over Mountains, Tech Note No. 34, WMO, Geneva, 135 pp.

Bretherton, F. P., 1969: Momentum Transport by gravity waves, Quart. J. Roy. Meteorol. Soc., 95, 213-243.

Coates, J. L., 1975: The NIMBUS-F Random Access Measurement System (RAMS), IEEE Trans. on Geoscience Electronics, GE-13, No. 1.

Donn, W. L. and N. K. Balachandran, 1973: Atmospheric gravity waves and the energy of the jet stream, Bull. Amer. Meteorol. Soc., 54, 633-636.

Eliassen, A. and E. Palm, 1960: On the transfer of energy in stationary mountain waves, Geofys. Publ., 22, 1-23.

Foldvik, A., 1962: Two-dimensional mountain waves--a method for rapid computations of lee waves lengths and vertical velocities. Quart. J. Roy. Meteor. Soc., 88, 271-285.

Gossard, E. E., 1962: Vertical Flux of Energy into the lower ionosphere from internal gravity waves generated in the Troposphere, J. Geophys. Res., 67, 745-757.

Hooke, W. H. and K. R. Hardy, 1975: Further study of the Atmospheric Gravity Waves over the Eastern Seaboard on 18 March 1969, J. Appl. Meteor., 14, 31-38. IEEE Transactions on Geoscience Electronics, 1975: Volume 13, No. 1.

Kung, E. C., 1967: Diurnal and Long-Term Variations of the Kinetic Energy Generation and Dissipation for a Five-Year Period, Mon. Wea. Rev., 95, 593-606.

Kung, E. C., 1969: Further Study of the Kinetic Energy Balance, Mon. Wea. Rev., 97, 573-581.

Lilly, D. K., 1972: Wave Momentum Flux-A GARP problem, Bull. Amer. Meteorol. Soc., 53, 17-23.

Lilly, D. K. and P. J. Kennedy, 1973: Observations of a stationary mountain wave and its associated momentum flux and energy dissipation, J. Atmos. Sci., 30, 1135-1152.

Lilly, D. K. and P. F. Lester, 1974: Waves and Turbulence in The Stratosphere, J. Atmos. Sci., 31, 800-812.

Lindzen, R. S., 1973: Wave Mean flow interactions in the upper troposphere, Boundary Layer Meteorol., 4, 327-343.

TWERLE Team, 1977: The TWERLE Experiment, Bull. of the Amer. Meteor. Soc., Vol. 58, No. 9, 936-948.

Uccellini, L. W., 1975: A case study of apparent gravity wave initiation of severe convective storms, Mon. Wea. Rev., 103, 497-513.

Van Loon, H., J. J. Taljaard, R. L. Jenne, and H. L. Crutcher, 1971: Climate of the Upper Air: Southern Hemisphere, Vol. II, Geostrophic Winds. NCAR-TN/STR-57, NCAR Boulder, Colorado.

Vergeiner, I., 1971: An Operational linear lee wave model for arbitrary basic flow and two-dimensional topography, Quart. J. Roy. Meteor. Soc., 97, 50-56.

Vergeiner, I. and D. K. Lilly, 1970: The dynamic structure of lee wave flow as obtained from balloon and airplane observations, Mon. Wea. Rev., 98, 220-232.